Journal of the Korean Physical Society, Vol. 68, No. 1, January 2016, pp. 41∼53

LiMn$_2$O$_4$-based Cathode Thin Films for Li Thin-film Batteries

Haena Yim, Dong-Wook Shin and Ji-Won Choi*
Electronic Materials Research Center, Korea Institute of Science and Technology, Seoul 02792, Korea

(Received 30 December 2014)

Substitution methods for Mn^{3+} in a spinel lithium manganese oxide with other cations have been used to prevent capacity degradation during the electrochemical charge and discharge of Li-batteries by increasing the average valence of Mn. In particular, in this review we outlin the effects of Sn substitution on the cycling performance of LiMn$_2$O$_4$ thin films that can be used as positive electrode in Li-batteries. The thin films were prepared by using pulsed laser deposition and solution deposition with regard to the structural and the electro-chemical characteristics.

PACS numbers: 73.50.-h
Keywords: LiMn$_2$O$_4$, Spinel, Lithium batteries, Sn substitution
DOI: 10.3938/jkps.68.41

I. INTRODUCTION

Over the past two decades, Lithium rechargeable batteries have enjoyed widespread use as a convenient power source for portable devices like mobile phones, laptop computers, cam-coders, *etc.* Their high energy density and power make possible the using portable electrics for a reasonable amount of time [1]. Recently, demands for higher power, energy density, and longer cycle life with reduced cost have been increasing as improved technology allows the creation of smaller electronics and integrated portable devices with micro-electro-mechanical system (MEMS). The development of semiconductor processing and circuit design technologies is accelerating the trend of creating lighter and smaller devices, which is resulting in decreases in electric power and capacity. Therefore, thin-film batteries viz. microbatteries, containing solid electrolytes, have been investigated by some leading companies in USA, Israel, Japan, Oak Ridge Micro-Energy (ORME), Cymbet, Excellatron, Power Paper, NEC, NTT, and others. The developments of these companies in these areas are shown in Table 1. Solid-state batteries are expected to fulfill the power, energy density, and rechargeability demands. Moreover, they have other advantages such as long shelf life, versatile size and shape and high thermal and vibrational stabilities, while not causing contamination due to the leakage of the liquid electrolyte, self-discharge, and internal evolution of gas for future-oriented uses.

The energy density of a thin-film battery, like conventional batteries, is mainly determined by the product of the voltage and the specific capacity of the cell, and these properties are primarily a function of the electrode materials in the cell. Intensive research has been carried out to develop LiCoO$_2$ thin films appropriate for all-solid-state batteries by using the currently-used cathode (positive electrode) material, LiCoO$_2$ [2–4]. However, due to the high cost of Co and the structural deterioration of LiCoO$_2$ when large amounts of Li are re-moved from LiCoO$_2$ (a natural part of the charge/discharge cycle), more recent research has focused on finding entirely new cathode thin films [5].

II. DISCUSSION

1. LiMn$_2$O$_4$ Cathode Material

One of the alternative cathode materials for thin film batteries is lithium manganese oxide, which is non-toxic, can be used at high cell voltage and is superior in terms of cost. The Mn ion in lithium manganese oxides can be in the various oxidation states [2–7], and oxidation states with 2-4 octahedral coordination has been focused most common material which is related with spinel or rock-salt structure by electrostatic attraction/repulsion of Mn-ion occupied vacant 16c site between oxygen and Li-ion. Among them, the LiMn$_2$O$_4$ has become a promising alternative cathode material. LiMn$_2$O$_4$ crystallizes in the normal spinel structure with a space group symmetry of Fd3m [8], in which the Li$^+$ and the Mn$^{3+/4+}$ ions occupy, respectively, the 8a tetrahedral and 16d octahedral sites of the cubic close-packed oxygen array (Fig. 1) to give a cation distribution of $(\mathrm{Li})_{8a}[\mathrm{M}_2]_{16d}\mathrm{O}_4$. While the interconnection of the 8a tetrahedral sites via the neighboring empty 16c octahedral sites offers reversible lithium-ion intercalation/deintercalation without struc-

---

[*] E-mail: jwchoi@kist.re.kr; Fax: +82-2-958-5559

Table 1. Companies producing thin-film batteries and their uses

Company	Developing contents
Power Paper	Smart active label loaded with alkaline battery
Oak Ridge Mirco-Energy (OKME)	Pilot-type thin-film battery Implanted medical devices
Infinite Power Solutions	Flexible thin-film battery for smart active label
Cymbet	Lithium thin-film battery for active RF-ID tag
Solicore	Thin-film type lithium polymer battery for Smart cards and active RF-ID tags
NEC	Organic radical battery
NTT	Thin-film lithium battery
GS Nanotech	Thin-film lithium battery for active RF-ID tags, biosensors and MEMS applications
Rocket Electric	Primary thin-film flexible battery

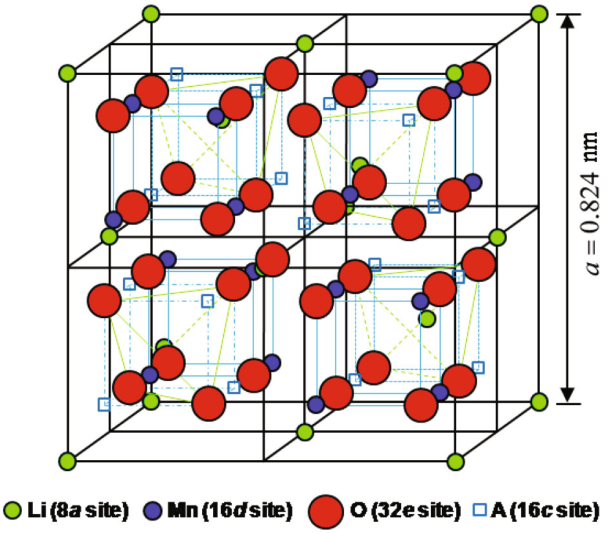

Fig. 1. (Color online) Crystal structure of spinel $LiMn_2O_4$ with LiO_4 tetrahedra and edge-shared MnO_6 octahedra.

tural collapse and fast three-dimensional lithium-ion diffusion (high σ_{Li}) within the strong covalently-bonded $[Mn_2]O_4$ framework, the edge-shared MnO_6 octahedra with a direct Mn-Mn interaction provide the good electronic conductivity, σ_e, needed for high-rate capability.

Unlike the layered $LiMO_2$ cathodes that suffer from the migration of transition-metal ions from the transition-metal layer to the lithium layer, the three-dimensional $[Mn_2]O_4$ spinel framework provides excellent structural stability, while supporting high-rate capability. Additionally, the lying of the $Mn^{3+}/^{4+}$: e_g band high above the O^{2-}: 2p band offers excellent chemical stability, unlike the $Co^{3+/4+}$ couple. Moreover, Mn is inexpensive and environmentally benign. As a result, $LiMn_2O_4$ with a discharge voltage of about 4 V [9] has become an appealing material for using a cathode.

Lithium ions are inserted/extracted from/into the 8a tetrahedral site at a voltage around 4 V which initial cubic spinel structure 1s maintained. However, only about 0.4 lithium ions per $LiMn_2O_4$ formula unit can be reversibly extracted, which limits the practical capacity to $<$ 120 mAh/g. Although an additional lithium could be inserted into the empty 16c sites of $(Li)_{8a}[M_2]_{16d}O_4$ at a voltage around 3 V versus Li/Li^+ to give the lithiated spinel $\{Li_2\}_{16c}[M_2]_{16d}O_4$, it is accompanied by a transformation of the cubic $(Li)_{8a}[M_2]_{16d}O_4$ (c/a = 1) into tetragonal $\{Li_2\}_{16c}[M_2]_{16d}O_4$ (c/a = 1.16) due to the Jahn-Teller distortion associated with the high spin Mn^{3+} : $3d^4$ $(t_{2g}{}^3e_g{}^1)$ ion. The Jahn-Teller theorem states that there cannot be unequal occupation of orbitals with identical energies. To avoid such unequal occupation, the molecule distorts so that these orbitals are no longer degenerate. For example, octahedral Mn (III), a d^4 ion, will experience the Jahn-Teller effect when only one electron occupies the e_g levels. This results in poor capacity retention during cycling in the 3-V region due to high volume changes caused by a ~6% increase in the unit cell volume, so the 3-V region cannot be utilized in practical cells. Correspondingly, the phase transition caused by the Jahn-Teller distortion occurs when the average valence state of manganese is below 3.5. Therefore, the phase transition can be restricted by specifically reducing the concentration of the Mn^{3+} ion in the as-prepared $LiMn_2O_4$ electrode.

In addition to the lower capacity ($<$ 120 mAh/g) when compared with that of the layered oxides, the $LiMn_2O_4$ spinel cathode encounters severe capacity fade even in the 4-V region (particularly at elevated temperatures). This has been attributed to a disproportionation of Mn^{3+} ions into Mn^{4+} and Mn^{2+} ions in the presence of trace amounts of hydrofluoric acid generated by a reaction of the $LiPF_6$ salt with the parts per-million-levels of water present in the electrolyte solution; while the Mn^{4+} ion remains as a solid, Mn^{2+} leaches out into the electrolyte and poisons the anode, resulting in capacity fade. The characteristics of $LiCoO_2$ and $LiMn_2O_4$ cathode materials, related to battery performance, are summarized in Table 2 for comparison.

Table 2. Comparison of $LiCoO_2$ and $LiMn_2O_4$ cathode materials.

Characteristics	$LiCoO_2$	$LiMn_2O_4$
Capacity limited (mAh/g)	120 − 130	100 − 120
Potential (V vs. Li/Li^+)	3.6	3.8
Fast charge time (h)	1.5 − 3	≤ 1
Load current (C-rate)	≤ 1	≤ 10
Cost (resource and battery control circuit)	Very high	Low
Environmental benignity	Poor	Good
O_2 evolution during overcharging	Yes	No
Safety	Bad (< 150 °C)	Good (< 250 °C)

2. Substitution of Mn

The focus of this review is the development of new high-cyclability thin-film electrodes by Sn substitution for Mn in spinel $LiMn_2O_4$ and understanding their electrochemical properties. The substitution of Mn^{3+} at the octahedral site of spinel $LiMn_2O_4$ by a substituting ion is necessary to increase the average valence state of Mn, so that the Jahn-Teller effect can be inhibited. Table 3 shows the toxicity and the ionic radii [10] of Mn^{3+}, Mn^{4+} and other substituting-ion candidates. The capacity retention with cycling in $LiMyMn_{2-y}O_4$ electrodes (M = Al [11], B [12], Ce [13], Co [14], Y [15], Cr [16], F [17], La [18], Nd [19], Mg [20], Ni [21], Sc [22], Se [23], Zn [24], *etc.*) has been reported to show better performance due to the increasing oxidation state (closer to Mn^{4+}: $3d^3$ ($t_{2g}{}^3e_g{}^0$)) of Mn ions. However, the doped $LiMn_2O_4$ provides a slightly lower initial discharge capacity because of the replacement of the Mn^{3+} ion by the substitution ion. Through comparison with previous studies, the replacement of Mn^{3+} by Sn^{2+} is especially beneficial to improve the cyclic performance of $LiMn_2O_4$ without the initial capacity loss due to the low content of the Mn^{3+} and with the non-toxicity of Sn compounds. The substitution is possible considering the ionic radii of Mn^{3+} and Sn^{2+}. Larger ions have been reported to be suitable for the substitution in octahedral site whereas smaller ions were suirable for substitution in tetrahedral sites [25,26]. Moreover, the ratio of the Sn^{2+}/O^{2-} ionic radius (0.132-nm ionic radius of O^{2-}) has in the range of 0.414 − 0.732, indicating that the coordination number must be six according to Pauling's first law. In addition, the study of Sn substitution in $LiMn_2O_4$ is worth investigating because unknown phenomena that have not been reported yet may exist.

Table 3. Toxicity and effective ionic radii of substituting-ion candidates for Mn^{3+} in $LiMn_2O_4$.

Ion	Toxicity^x	Effective ionic radius (Å)	Remarks to ionic radius^y
Mn^{3+}	b	0.785	R*
Mn^{4+}	b	0.670	R*
Monovalent			
Cu	a	0.77	E
Li	a	0.76	*
Divalent			
Co	a	0.745	R*
Cr	a	0.80	R
Cu	a	0.73	
Fe	b	0.780	R*
Ge	a	0.73	A
Mg	b	0.720	*
Ni	c	0.690	R*
Pd		0.86	
Pt		0.80	A
Sn	b	0.93	
Ti	a	0.86	E
V	c	0.79	
Zn	b	0.740	R*
Trivalent			
Ag	b	0.75	R
Au		0.85	A
In	b	0.800	R*
Lu	b	0.861	R
Mo	a	0.69	E
Nb	b	0.72	
Pd		0.76	
Ru	b	0.68	
Sb	c	0.76	A
Sc	b	0.745	R*
Ta	b	0.72	E
Tb	b	0.923	R
Ti	a	0.670	R*
Tl	c	0.885	R
Tm	b	0.880	R
Y	b	0.900	R*
Yb	b	0.868	R*
Tetravalent			
Am	c	0.85	R
Bk		0.83	R
Ce	b	0.87	R
Cf		0.821	R
Cm		0.85	R
Hf	b	0.71	R

Ion	Toxicity[x]	Effective ionic radius (Å)	Remarks to ionic radius[y]
Mo	a	0.650	RM
Nb	b	0.68	RE
Np	c	0.87	R
Pa	c	0.90	R
Pb	c	0.775	R
Pr	b	0.85	R
Pu	c	0.86	R
Sn	b	0.69	R
Ta	b	0.68	E
Tb	b	0.76	R
U	c	0.89	
Zr	b	0.72	R*

[x] a: nontoxic, b: slightly toxic, and c: toxic.
[y] R: from r^3 vs. V plots, E: estimated, * most reliable, M: from metal oxides, A: anticipated

3. Sn-substituted LiMn$_2$O$_4$ Thin Films Prepared by PLD

Preparation of targets. Target materials of LiSn$_{x/2}$Mn$_{2-x}$O$_4$ ($x = 0$, 0.025 and 0.05) were prepared by using the conventional solid-state reaction. Raw material, Li$_2$CO$_3$ ($\geq$ 99%, Aldrich), MnO$_2$ ($\geq$ 99%, Aldrich), and SnO ($\geq$ 99%, Aldrich) or SnO$_2$ (99.9%, Aldrich) in a stoichiometric proportion, were ball-milled in an anhydrous ethanol medium for 20 h. After the powder had been dried at 120 °C for 24 h, it was ground and was then calcined at 700 °C for 5 h. The calcined powder was ground again and then thoroughly mixed with a few drops of a 0.05 wt% solution of poly(vinyl alcohol) (PVA). The mixture was uniaxially pressed at 490 MPa to form a pellet and then finally sintered at 1200 °C for 2 h. The fired targets were characterized at a fired density of ~3.5 g/cm^3, ~82% of the theoretical density (4.281 g/cm^3) [27] as measured by the Archimedes method, and a shrinkage of -1%, regardless of target composition.

Preparation of Sn-substituted LiMn$_2$O$_4$ thin films. Thin films were prepared for 45 min on a Pt/Ti/SiO$_2$/Si(100) substrate (10 × 10 mm^2) by using the PLD method with a KrF excimer laser (wave length, $\lambda = 248$ nm and pulse width, $\tau = 25$ ns). The base pressure of the chamber for the PLD was lower than 10^{-3} Pa. The conditions used for deposition are as follows: (i) laser energy density: 4.6 J/cm^2, (ii) pulse frequency: 10 Hz, (iii) target-substrate distance: 4 cm, (iv) working (oxygen) pressure: 26.7 Pa, and (v) substrate temperature: 450 °C.

Structural analyses. An X-ray diffractometer (Rigaku RINT 2000) using Cu $K\alpha$ radiation was used at a scan rate of 1 deg/min for the refinements and phase analyses in this review. A secondary electron microscope (FEI XL-30 FEG) was used for the morphological study of all the films in this review. The analysis of NEXAFS (near edge X-ray absorption fine structure) was carried out at the 7Ba KIST (Korea institute of science and technology) beamline of the PLS (Pohang Light Source) 2.5-GeV storage ring by using a soft X-ray absorption spectroscope (XAS) equipped with a VLS PGM monochromator (80 $-$ 1500 eV) operating at the carbon K edge with an energy resolution of 0.2 eV.

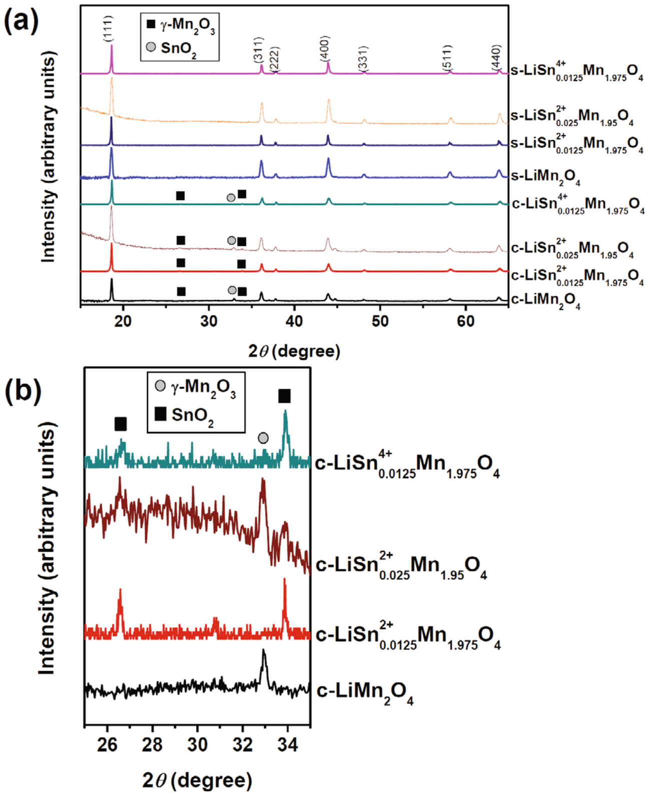

Fig. 2. (Color online) X-ray diffraction patterns of (a) LiM$_{x/2}$Mn$_{2-x}$O$_4$ (M = Sn^{2+} and Sn^{4+}, $x = 0$, 0.025 and 0.05) powders fired at 700 °C for 5 h and then at 1200 °C for 2 h and (b) magnified X-ray diffraction patterns of LiM$_{x/2}$Mn$_{2-x}$O$_4$ (M = Sn^{2+} and Sn^{4+}, $x = 0$, 0.025 and 0.05) powders fired at 700 °C for 5 h. The sintered powders are single-phased according to XRD regardless of the Sn content and the valence state of Sn.

Electrochemical measurements. Electrochemical measurements unit in this review were carried out by using a lab-made half-cell with the following conditions: The electrolyte consisted of a 1-M solution of LiPF6 dissolved in a 1:1 vol% solvent of ethylene carbonate (EC) and diethyl carbonate (DEC). The counterelectrode was a lithium foil (10 × 10 mm^2, 0.38-mm thick). The charge/discharge was performed at a current rate of 330 mA/g at voltage between 3.0 and 4.5 V.

Characterization of LiSn$_{x/2}$Mn$_{2-x}$O$_4$ target materials. The prepared targets of LiM$_{x/2}$Mn$_{2-x}$O$_4$ (M = Sn^{2+} and Sn^{4+}, $x = 0$, 0.025 and 0.05) sintered at 1200 °C for 2 h were characterized as having a cubic cell with

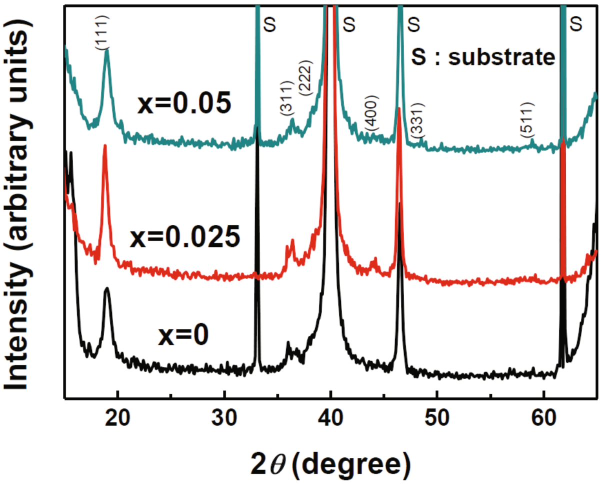

Fig. 3. (Color online) X-ray diffraction patterns of various thin films showing the effect of Sn substitution in the LiMn$_2$O$_4$-based compound. Thin films containing element Sn in the stoichiometry LiSn$_{x/2}$Mn$_{2-x}$O$_4$ (x = 0, 0.025 and 0.05) as-deposited by using PLD are single-phased according to XRD. Copyright 2008 American Institute of Physics [41].

space group $Fd\bar{3}m$, as evidenced by the X-ray powder diffraction refinements in Fig. 2 [5,27–40]. In Fig. 2, the c-LiSn$_{x/2}$Mn$_{2-x}$O$_4$ is powder after the calcining, and the s-LiSn$_{x/2}$Mn$_{2-x}$O$_4$ is powder after the sintering. Some impurity phases, such as SnO$_2$ and γ-Mn$_2$O$_3$, were found after the calcining. After the final sintering process at 1200 °C for 2 h, no secondary phase was found. Therefore, it was assumed that Sn could be incorporated into the spinel LiMn$_2$O$_4$-based structure. In this structure, the Li occupies the 8*a* tetrahedral sites, the Mn occupies the octahedral (16*d*) sites and the oxygen forms a face-centered cubic array with 32*e* sites, while the other octahedral site (16*c*) is vacant [28]. Therefore, the intense reflection peaks are indexed according to the literature [27,29].

Characterization of LiSn$_{x/2}$Mn$_{2-x}$O$_4$ thin films. As expected, the XRD patterns of the LiSn$_{x/2}$Mn$_{2-x}$O$_4$ thin films, show in Fig. 3, showed the identical cubic phase with space group $Fd\bar{3}m$ regardless of the Sn content. Sn^{2+} seemed to be accommodated into the LiMn$_2$O$_4$ structure as only the LiMn$_2$O$_4$ spinel phase was observed even for the LiSn$_{0.025}$Mn$_{1.95}$O$_4$ thin film. The Sn ion is assumed to have substituted for the Mn ion in the 16*d* octahedral site of the spinel.

Figure 4(a) shows the surface microstructures of as-prepared LiSn$_{x/2}$Mn$_{2-x}$O$_4$ (x = 0, 0.025 and 0.05) thin films at high magnification, in which all surfaces were identical regardless of Sn content. Figure 4(b) shows the surface microstructures of as-prepared LiSn$_{x/2}$Mn$_{2-x}$O$_4$ (x = 0, 0.025 and 0.05) thin films at low magnification. The large particulates and the rough surfaces seen in Fig. 4(b) imply that the laser energy density of 4.6 J/cm^2 was too high. The rough surface, caused by the high laser energy density, was assumed to have resulted in the degradation of the electrochemical performances due to the concentration at charge in the sharp points on the film surface.

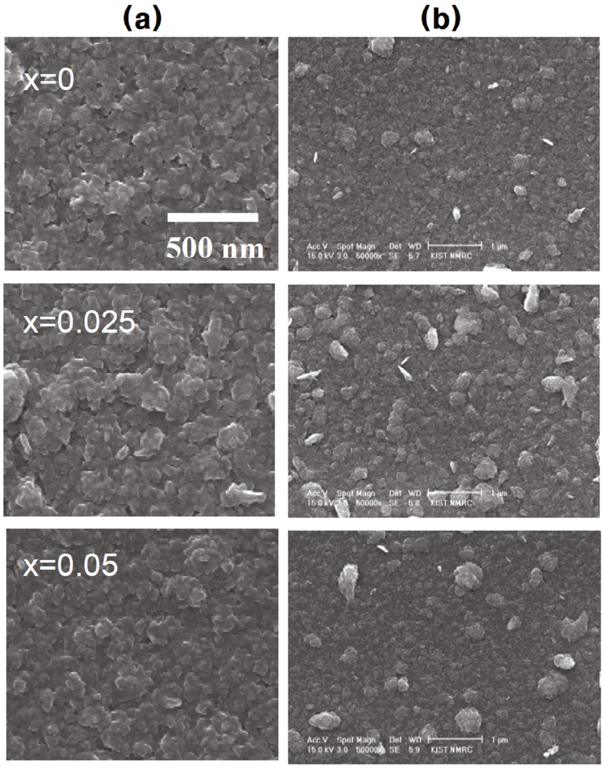

Fig. 4. SEM images for the surfaces of as-prepared LiSn$_{x/2}$Mn$_{2-x}$O$_4$ (x = 0, 0.025 and 0.05) thin films at (a) high magnification and (b) low magnification.

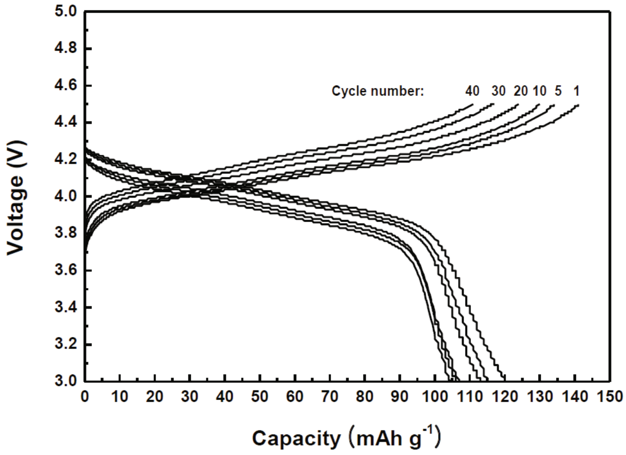

Fig. 5. Voltage−capacity profiles for the as-prepared LiSn$_{0.0125}$Mn$_{1.975}$O$_4$ thin films galvanostatically cycled at a current rate of 330 mA/g. (Copyright 2008 American Institute of Physics [52]).

Figure 5 shows the voltage profiles for the 1st, 5th, 10th, 20th, 30th, and 40th cycle for the LiSn$_{0.0125}$Mn$_{1.975}$O$_4$ thin film. No distinct plateau was seen in the 4 V regions, a promising result of the cy-

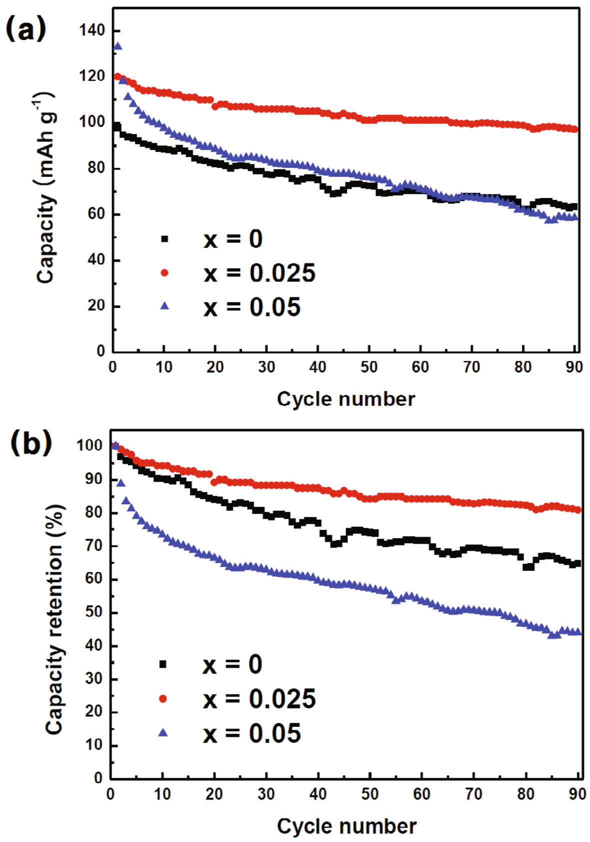

Fig. 6. (Color online) (a) Discharge capacity and (b) capacity retention of $LiSn_{x/2}Mn_{2-x}O_4$ (x = 0, 0.025 and 0.05) thin films galvanostatically cycled at a current rate of 330 mA/g until the 90th cycle. (Copyright 2008 American Institute of Physics [52]).

cling evaluation. The occurrence of a plateau is known to often induce unstable operation and electrical breakdown [42]. Figure 6 shows capacity plots of the thin films as a function of the number of cycles. In particular, the $LiSn_{0.0125}Mn_{1.975}O_4$ thin film showed an improved initial discharge capacity of ∼120 mAh/g, which is much higher than the voltage of ∼100 mAh/g for the undoped $LiMn_2O_4$ thin film. The capacity retention of the $LiSn_{0.0125}Mn_{1.975}O_4$ film was 81% of the first discharge capacity after 90 cycles at the higher current rate of 330 mA/g corresponding to an approximate rate of 4 C. The 4 C rate is much higher than the regular one reported in the literature [43, 44]. The improved capacities of the Sn-substituted thin films are believed to be associated with the increase in the number of site available for the lithium intercalation/deintercalation in the manganese-deficient $LiSn_{x/2}Mn_{2-x}O_4$ structure [45]. The shortening of the Mn-O bond length by Sn substitution seems to cause migration of the lithium ion into the spinel structure easier because it increases the space for the 8*a* tetrahedral and the 16*c* octahedral sites for the lithium intercalation/deintercalation [46].

For the case of $LiSn_{0.025}Mn_{1.95}O_4$ with a higher Sn substitution, the observed lower cyclability of 44% is assumed to have been induced by the excessive Sn, which leads to interference with the Mn^{3+}-Mn^{4+} conduction paths and the inhomogeneous occurrence of charge-discharge [47,48]. As a similar case, studies of yttrium-substituted $LiMn_2O_4$ has found that the excessive substitutions of Y damaged the cyclability seriously [49].

Figure 7(a) illustrates the Mn *K*-edge X-ray absorption spectra of as-prepared and cycled $LiMn_2O_4$ and $LiSn_{x/2}Mn_{2-x}O_4$ films as compared to standard samples of MnO (Mn^{2+}) and MnO_2 (Mn^{4+}). Based upon the calculation [50] of the molecular excited states of $(FeO_6)^{-10}$ and the experimental results of the Mn_2O_3, MnO_2 and $LiMn_2O_4$ powders [51], we ascribe the weak pre-edge peaks A_1 and A_2 in all samples to quadruple transitions from 1*s* into the final 3*d* states of t_{2g} and e_g symmetry. The shoulder B in Fig. 7(a) is also assigned to excitation from the Mn 1*s* to a *p*-like state of t_{1u} symmetry. From the observation of two different B_1 and B_2 absorption peaks, one can easily conjecture that two different Mn sites (Mn^{3+} and Mn^{4+}) coexist in the spinel structure of $LiMn_2O_4$ and $LiSn_{x/2}Mn_{2-x}O_4$. The other peaks, C and D, may arise from the shape resonance in the continuum part of the spectrum and from multiple scattering resonances. With respect to the energy separations between the peak of B (the mean energy position of B_1 and B_2) and the peak of C shrinking in all-cycled $LiMn_2O_4$ and $LiSn_{x/2}Mn_{2-x}O_4$ samples, the cause may be related to the change in the interatomic distance and the site symmetry over the repeated Li intercalation/deintercalation. Figure 7(b) shows the O-*K* edge NEXAFS spectra of the as-prepared and cycled $LiMn_2O_4$, and $LiSn_{x/2}Mn_{2-x}O_4$ samples. In Fig. 7(b), the spectrum can be divided into two regions: the first region below the energy of 535 eV (labeled O_1, O_2) and the second region above 535 eV with an additional structure (O_3-O_5). According to molecular orbital pictures, O_1 and O_2 are generated by the excitation from the O 1*s* core level into the t_{2g} and eg bands, respectively, and the peaks at the higher energies (O_3-O_5) are due to the transitions to antibonding O 2*p* and Mn 4*s*- and 4*p*-related bands. When the spectra of the as-prepared and the cycled samples are compared, two highly interesting points arise. The first is the slight shift of the nearly 1 V toward the higher binding energies of the e_g, level along with the broadening of ligand-field splitting (10 Dq) from 1.1 to 1.8 eV after the cycle test. The second is the disappearance of the O_1 peak in the cycled $LiMn_2O_4$ and $LiSn_{0.025}Mn_{1.95}O_4$ samples, not in the $LiSn_{0.0125}Mn_{1.975}O_4$ sample. Such an energy shift and broadening typically occur due to variations in the bond lengths and angle local in the local crystalline structures of spinel lithium manganese oxide, as previously observed in TiO_2 with similar crystalline symmetry [53]. This result is in good agreement with the fact that the eg orbitals are more sensitive to the local environment then the t_{2g} orbitals. Although the relative intensity of t_{2g}/e_g becomes low in the cycled $LiSn_{0.0125}Mn_{1.975}O_4$ sample,

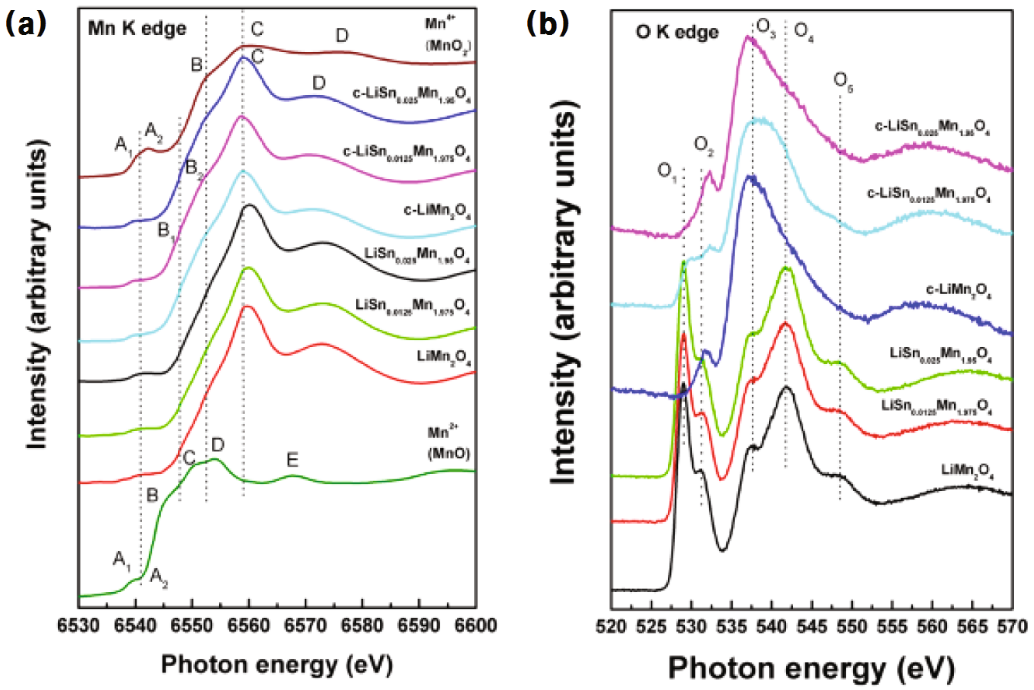

Fig. 7. (Color online) Chemical valence change analysis. Shown here is the near-edge X-ray absorption fine structure (NEXAFS) spectra of $LiSn_{x/2}Mn_{2-x}O_4$ ($x = 0$, 0.025 and 0.05) thin films before and after cycle tests: (a) the Mn K edge. And (b) O K edge. (Copyright 2008 American Institute of Physics [52]).

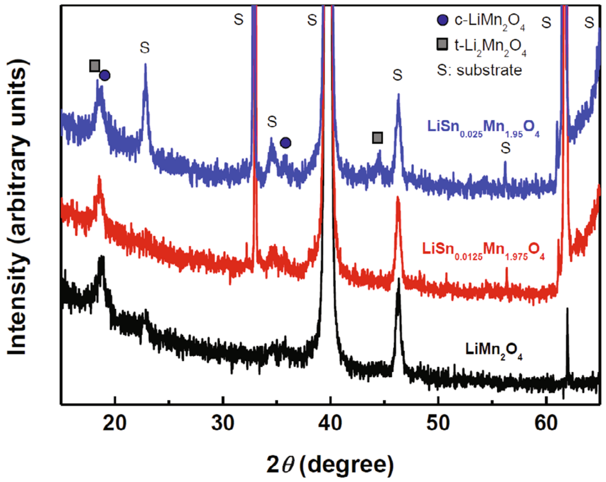

Fig. 8. (Color online) X-ray diffraction patterns of pulsed-laser-deposited thin films showing the effect of Sn substitution on phase transition after a long cycle test. Thin films containing Sn elements in the stoichiometry $LiSn_{x/2}Mn_{2-x}O_4$ ($x = 0.025$) showed little phase transition according to XRD [52].

the existence of the t_{2g} peak in $LiSn_{0.0125}Mn_{1.975}O_4$ is closely related to the improved cyclability and can serve as a feasible criteria for determining when the degradation initiates in the cyclability test.

Figure 8 shows the XRD patterns of pulsed-laser-deposited $LiSn_{x/2}Mn_{2-x}O_4$ ($x = 0$, 0.025 and 0.05) thin films after a long cycle test. The $LiSn_{0.0125}Mn_{1.975}O_4$ thin film showed the least phase transition from cubic to tetragonal caused by the Jahn-Teller distortion. The phase transition to tetragonal in the thin films of $LiSn_{x/2}Mn_{2-x}O_4$ ($x = 0$ and 0.05) during cycling was noticeable, as evidenced by the peaks of $Li_2Mn_2O_4$ impurities and the deviation of the main (111) peak at around 18.6° in the XRD patterns.

Figure 9 shows the surface microstructures of $LiSn_{x/2}Mn_{2-x}O_4$ ($x = 0$, 0.025 and 0.05) thin films after a long cycle test. Manganese dissolution was shown to have occurred due to structural degradation caused by the Jahn-Teller distortion and the disproportionation reaction. Especially, the cycled thin films of $x = 0$ and 0.05 showed much the dissolution of the film and many precipitated particles. The precipitated particles in pulsed-laser-deposited $LiMn_2O_4$ thin films after cycling are known to be result corresponding to cyclic degradation [54].

Sn-substituted $LiMn_2O_4$ thin films prepared by using pulsed laser deposition showed an exceptionally strong cyclability, which is highlighted by the capacity retention of ~81% at the unusually high current rate of ~4 C. The films also showed a higher initial capacity of 120 mAh/g. These promising values are preferred as for the active materials that is to be used as an anode for a thin film lithium battery.

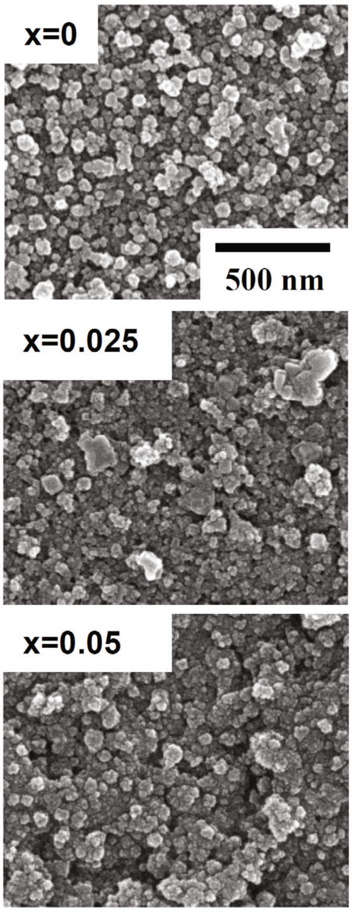

Fig. 9. SEM images for the surfaces of pulsed-laser-deposited $LiSn_{x/2}Mn_{2-x}O_4$ ($x = 0$, 0.025 and 0.05) thin films after a long cycle test.

4. Sn-Substituted $LiMn_2O_4$ Thin Films Prepared by Solution Deposition

Preparation of starting solutions. Lithium acetylacetonate $CH_3COCH{=}C(OLi)CH_3$ (97%, Aldrich), manganese (III) acetylacetonate $Mn(C_5H_7O_2)_3$ (technical grade, Aldrich), and tin (II) acetate $Sn(CH_3CO_2)_2$ (Aldrich) were completely dissolved into a common solution of 1-butanol ($\geq$ 99%, Junsei) and acetic acid ($\geq$ 99.7%, Aldrich) by stirring for 20 h. The concentration of the starting solutions was fixed at 0.3 M.

Film formation by spin-coating. Thin films were prepared on $Pt/Ti/SiO_2/Si(100)$ substrates (10×10 mm^2) by using solution deposition, viz. spin-coating with the 0.3-M starting solution. The spin-coating was performed at 4000 rpm for 30 s. The steps of spin coating and preheating at 310 °C were repeated up to eight times. The films were finally annealed at 750 °C for 5 min in an O_2 atmosphere by using a rapid thermal processor (KVT, KVRTA-R40). The thickness of films was ∼140 nm.

Microstructural analyses. The surface roughness of the $LiSn_{x/2}Mn_{2-x}O_4$ thin films were observed by using atomic force microscopy (AFM) (Veeco, Dimension 3100).

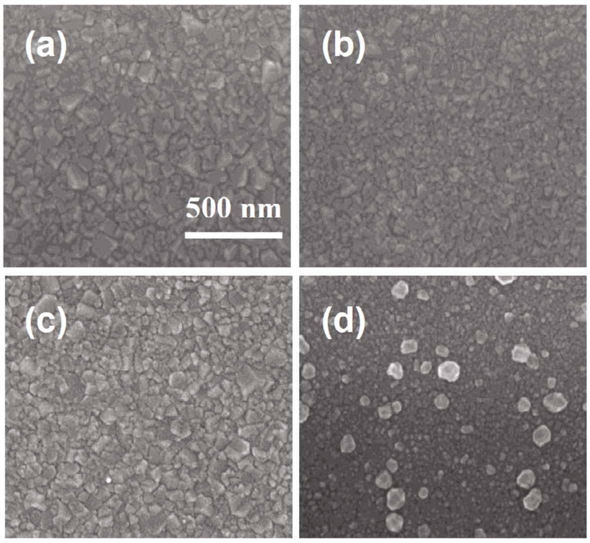

Fig. 10. SEM images for the surfaces of $LiSn_{x/2}Mn_{2-x}O_4$ thin films showing the microstructure caused by Sn substitution: (a) $x = 0$, (b) $x = 0.05$, (c) $x = 0.1$, and (d) $x = 0.2$.

Electrochemical measurements. The charge/discharge was performed at a current rate of 300 mA/g at voltage between 3.0 and 4.5 V.

Spectroscopic analyses. XPS spectra were collected on a PHI 5800 ESCA system with a monochromatic Al $K\alpha$ (1486.6 eV) anode (250 W, 10 kV, 27 mA). The deconvolutions of the narrow scan peaks of the Mn $2p$ and the Sn $3d$ core-levels related to each portion of Mn^{3+}, Mn^{4+}, Sn^{2+}, and Sn^{4+} were performed by using the program SDP 4.0 (XPS international, LLC) by using the Shirley baseline and the 90/10% ratio of Gaussian/Lorentzian function. Mn K-edge X-ray absorption spectra were recorded at the 3C1 beamline at the Pohang Light Source (PLS) with a ring current of 130 − 185 mA at 2.5 GeV. A Si(111) double-crystal monochromator was employed. All spectra were recorded in the transmission mode with a N_2-filled ionization chamber and were calibrated by checking the first inflection point of the Mn foil with the reference Mn K edge = 6539 eV. Fourier transformations (FTs) were performed by using k^2 weighting. The theoretical parameters used in the curve-fitting analysis were calculated by using the program FEFF 7.0. An X-ray diffractometer (Rigaku, RINT 2000) with Cu $K\alpha$ radiation was used for phase identification.

Microstructures of thin films. Figure 10 shows the surface microstructures of as-prepared $LiSn_{x/2}Mn_{2-x}O_4$ thin films. All surfaces showed clear granular structures with relatively uniform grain sizes. Grain size depended on the content of Sn. Specifically, the $x = 0.05$ sample exhibited a very uniform distribution of smaller grains. Figure 11 represents the RMS (root mean square) values

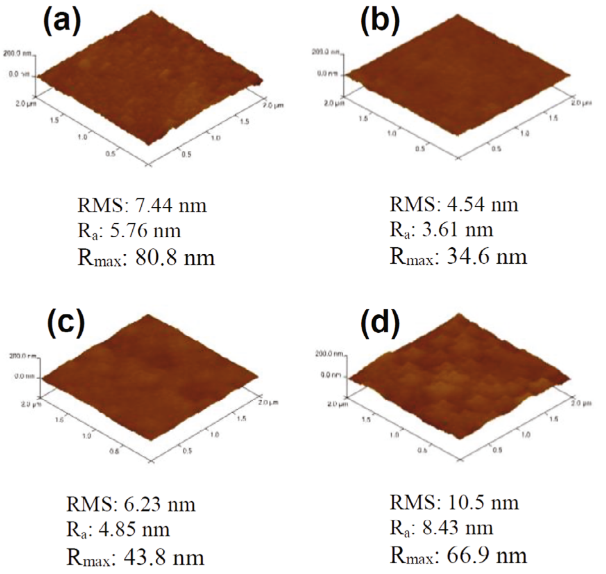

Fig. 11. (Color online) AFM images for the surfaces of LiSn$_{x/2}$Mn$_{2-x}$O$_4$ thin films showing the surface roughness due to Sn substitution: (a) x = 0, (b) x = 0.05, (c) x = 0.1, and (d) x = 0.2.

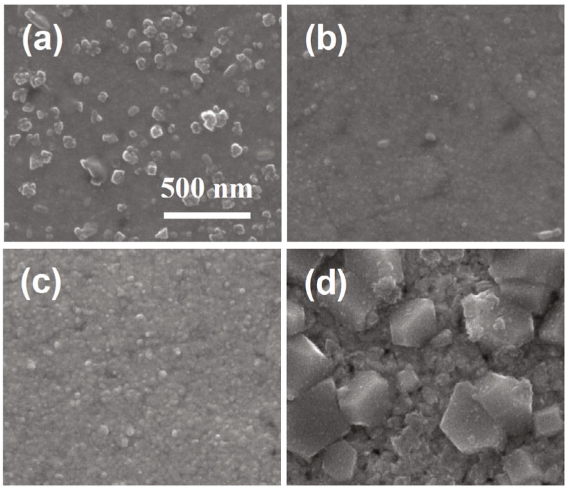

Fig. 12. SEM images for the surfaces of LiSn$_{x/2}$Mn$_{2-x}$O$_4$ thin films showing the microstructural variation after a long cycle test: (a) x = 0, (b) x = 0.05, (c) x = 0.1, and (d) x = 0.2.

measured by using AFM for the thin films containing different Sn contents. These values match well with the variation of the grain size. For instance, the x = 0.05 sample showed the lowest RMS value of 4.54 nm, which corresponded to smaller grain sizes. A large content of Sn was assumed have formed an impurity, as shown in Fig. 10(d).

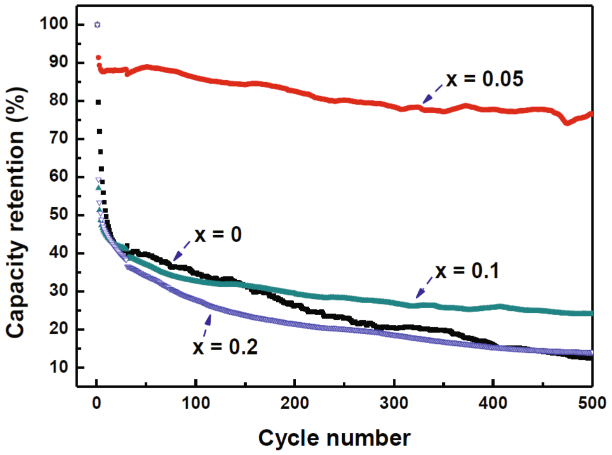

Fig. 13. (Color online) Capacity retention of LiSn$_{x/2}$Mn$_{2-x}$O$_4$ thin films up to 500 cycles. (Copyright 2009 Elsevier B. V [55]).

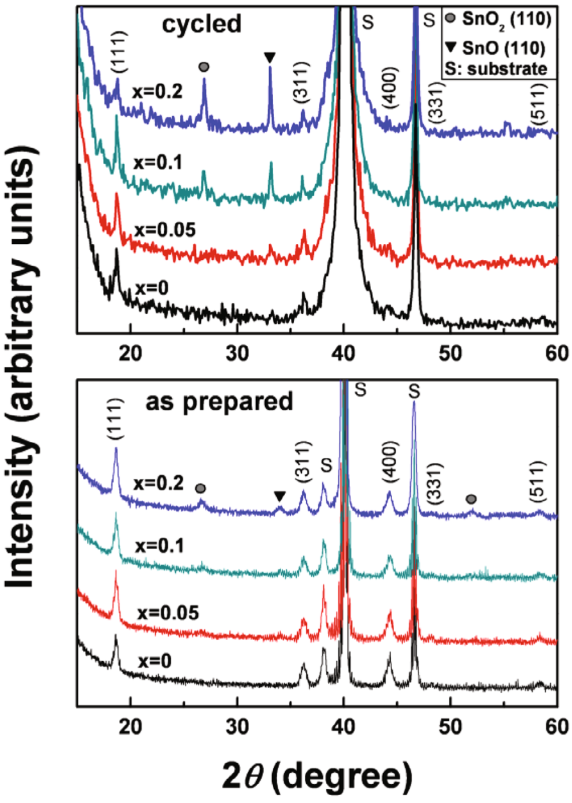

Fig. 14. (Color online) XRD patterns of LiSn$_{x/2}$Mn$_{2-x}$O$_4$ thin films as prepared and after the third cycle. (Copyright 2009 Elsevier B. V) [55].

Figure 12 shows the surface microstructures of harshly-cycled LiSn$_{x/2}$Mn$_{2-x}$O$_4$ thin films. The films were dissolved in the liquid electrolyte; consequently, the surface of Pt was revealed, except for the x = 0.05 sample. The cycled film with x = 0.2 in Fig. 12(d) showed severe collapse of the film structure and precipitated particles. Therefore, the film with x = 0.05 was assumed to be the most resistive to Mn dissolution and capacity degradation.

Electrochemical and physical properties of

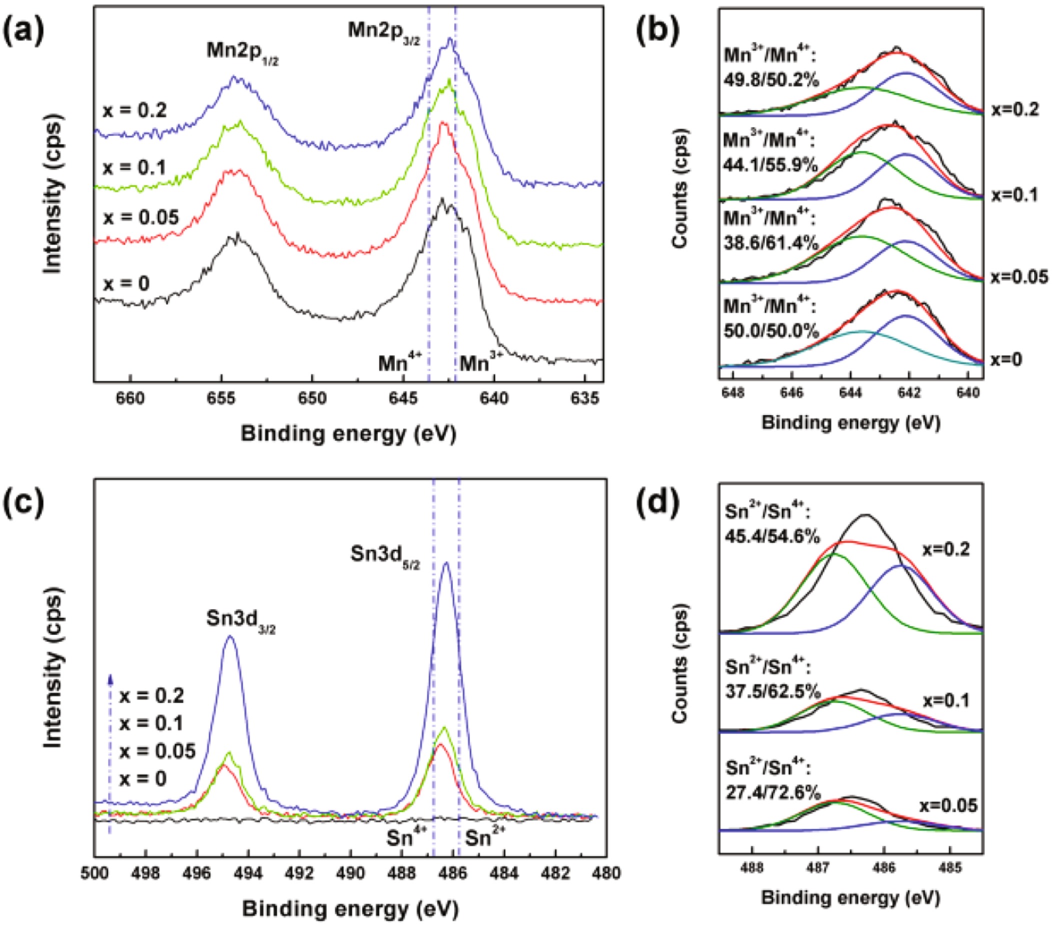

Fig. 15. (Color online) (a) Mn 2p XPS spectra, (b) deconvoluted profile of specific Mn $2p_{3/2}$ XPS spectra, (c) Sn 3d XPS spectra, and (d) deconvoluted profile of specific Sn $3d_{5/2}$ XPS spectra of $LiSn_{x/2}Mn_{2-x}O_4$. (Copyright 2009 Elsevier B. V [55]).

thin films. Figure 13 shows the cyclability of $LiSn_{x/2}Mn_{2-x}O_4$ thin films (x = 0, 0.05, 0.1, and 0.2) up to 500 cycles. The capacity retention of the x = 0.05 thin film was 77% of the first discharge capacity after 500 cycles at the higher current rate of 10 C. The high current rate of 10 C, which corresponds to a current rate of 300 mA/g, has been found to differentiate cyclability among samples.

Figure 14 shows the X-ray diffraction patterns of $LiSn_{x/2}Mn_{2-x}O_4$ thin films prepared by using the solution deposition process before and after the third cycle. All films were shown to have the identical cubic phase with space group $Fd\bar{3}m$ regardless of Sn content. No distinguishable secondary phase was observed at x = 0.05. When the Sn content was $x \geq 0.1$, however, precipitation peaks of both SnO_2 (110) and SnO (110) were observed. The precipitation peaks of SnO_2 (110) and SnO (110) were apparently observed for the samples of $x \geq 0.1$ after the cycling test. SnO_2 and SnO are thought to have been precipitated as an accompanying result of the Mn dissolution, as well as SnO_2 and SnO located outside the $LiMn_2O_4$ lattice, which originated from the disproportionation reaction during the cycling test [56]. The disproportionation reaction was reported in other similar systems including yttrium-doped spinel $LiMn_2O_4$, where the substituting ions facilitated the dissolution of Mn [34].

Figure 15(a) shows the XPS spectra of the Mn $2p_{1/2}$ and the Mn $2p_{3/2}$ core levels of $LiSn_{x/2}Mn_{2-x}O_4$ thin films which result from the spin-orbit splitting. The FWHM (full width at half maximum) larger than 3.5 eV for all the Mn $2p_{3/2}$ peaks explicitly indicates coexistence of mixed Mn^{3+} and Mn^{4+} ions over the substitution range of Sn. The Deconvoluted Mn XPS profiles in Fig. 15(b) denote the percentages of manganese content that can be used to calculate the average valance states of Mn between Mn^{3+} and Mn^{4+}. Deconvolution was precisely carried out with the binding energy positions of Mn^{3+} and Mn^{4+} being fixed at 642.1 eV and 643.6 eV, respectively, and with a FWHM lower than 4.0 eV. The x = 0.05 sample can be highlighted with a valence state of 3.61, which is higher than the 3.50 value of pure thin films, and the valance state becomes small as low as 3.56 and 3.50, at higher Sn contents of x = 0.1 and 0.2, respectively. Such a slight increase in valence state for the $x = 0.05$ sample is assumed to be associated with the replacement of Mn^{3+} in the octahedral site ($16d$) with Sn^{2+} ($Sn_{Mn}^{'}$) and with a Mn vacancy ($V_{Mn}^{'''}$) to maintain charge neutrality.

Figure 15(c) shows the XPS spectra of the Sn $3d_{3/2}$ and the Sn $3d_{5/2}$ core levels of $LiSn_{x/2}Mn_{2-x}O_4$ thin films which result from the spin-orbit splitting. The peak points of both the $Sn3d_{3/2}$ and the $Sn3d_{5/2}$ core levels are shifted to lower binding energies as the Sn content is increased. This tendency means that the relative content of Sn^{2+} is more than that of Sn^{4+} at higher Sn contents. The percentage of Sn content can be identified more definitely from the deconvolution profiles in Fig. 15(d). The deconvolution was precisely carried out at fixed the binding energy positions of Sn^{2+} and Sn^{4+} at 485.75 eV and 486.75 eV with the FWHM, respectively lower than 1.4 eV [57].

If all components of Sn^{2+} and Sn^{4+} substitute for Mn, the average valence states of Mn, based on calculations using the Sn deconvolution data in Fig. 15(d) are 3.62, 3.71, and 3.91 at $x = 0.05$, 0.1, and 0.2, respectively. This behavior of the average charge state of Mn can be understood by comparing the ionic radii of Sn and Mn because the relation of the ionic radii is Sn^{2+} (0.930 Å) $>$ Mn^{3+} (0.785 Å) $>$ Sn^{4+} (0.690 Å) $>$ Mn^{4+} (0.670 Å) [10]. Considering the charge affinities and the sizes of Sn and Mn ions, Sn^{2+} and Sn^{4+} can effectively substitute for Mn^{3+} and Mn^{4+}, respectively. The average valence of Mn increases when Sn^{2+} substitutes for Mn^{3+} whereas that of Mn decreases when Sn^{4+} substitutes Mn^{4+}. As shown in Fig. 14, the intensity of the SnO (110) peak increases at a higher rate than that of SnO_2 (110) peak does with increasing Sn content. This means that a small amount of Sn^{2+} substitutes for Mn^{3+} at a limited solubility and that most of the Sn^{2+} is located outside $LiMn_2O_4$ lattice due to the large ionic radius of Sn^{2+}. On the other hand, more Sn^{4+} is assumed to substitute for Mn^{4+} than Sn^{2+} for Mn^{3+}. Therefore, the average valence state of Mn decreases at $x \geq 0.1$.

Figure 16 shows the Fourier transform (FT) magnitudes of k^2-weighted Mn K-edge extended X-ray absorption fine structure spectra of $LiSn_{x/2}Mn_{2-x}O_4$ thin films (x = 0, 0.05, and 0.1). The first two prominent peaks around 1.3 Å and 2.4 Å are generated by simple backscattering of photoelectrons from the first coordination shell of six oxygen atoms (Mn−O) and the second coordination shell of cations occupying the six neighboring $16d$ octahedral sites (Mn−Mn) [58]. As shown in Fig. 16, the intensity of the nearest-neighbor Mn−O bond is greatly influenced by the Sn content, but that of the Mn(Sn)−Mn bond [58,59] shows no change as Sn content is varied from $x = 0.05$ to $x = 0.1$. From the inset of Fig. 16, the intensity of the Mn-O bond shows a maximum at $x = 0.05$ and then is attenuated close to that of pure $LiMn_2O_4$ at $x = 0.1$. The peak intensity and the broadness of FT spectra are known to depend on the coordination number and the Debye-Waller factors, which reflect thermal vibration and/or distortion of bond. In this experiment, the variations of the peak intensity mainly correlated to the distortion of Mn−O octahedra because the temperature did not change. The intensified peak of the Mn−O bond as shown in Fig. 16, is related to both the increase in the Mn valence state and the decrease in the local distortion around Mn ions due to the Sn substitution [60]. Two possibilities exist to increase the Mn valence through replacement of Mn^{3+} by either Sn^{2+} or Sn^{4+} for keeping electroneutrality. In this process, the probability of replacing Mn^{3+} by Sn^{2+} will be lower than replacing Mn^{2+} by Sn^{4+} due to the large ionic radius of Sn^{2+}. Simultaneously, Sn^{4+} can more easily replace Mn^{4+} because of very similar ionic radii between Sn^{4+} and Mn^{4+}, and this is more probable than the replacement of Mn^{3+} by Sn^{2+} or Sn^{4+}. As Sn content increases, the increase in the Sn^{4+}−O bond results in a homogeneous distribution of the M−O bond length, but this reversely decreases the whole valence of Mn. As a consequence, when doping with a small amount of Sn ($x = 0.05$), the distortion of MO_6 (M = Sn and Mn) octahedral can be suppressed by Sn^{2+} and Sn^{4+} doping for Mn^{3+} in $LiSn_{x/2}Mn_{2-x}O_4$ and the Mn valence. However, the probability of replacing Mn by Sn^{2+} is quite lower compared to that of replacing Mn by Sn^{4+}. The Sn substitution up to $x = 0.05$ is suggested to impose an optimal enhanced static ordering of Mn and Sn in each coordination shell of the spinel structure. The suppression of distortion at further Sn substitution above $x = 0.05$, however, seems to be quite weakened due to the decrease in the Mn valence due to the increase in absolute amount of SnO_2.

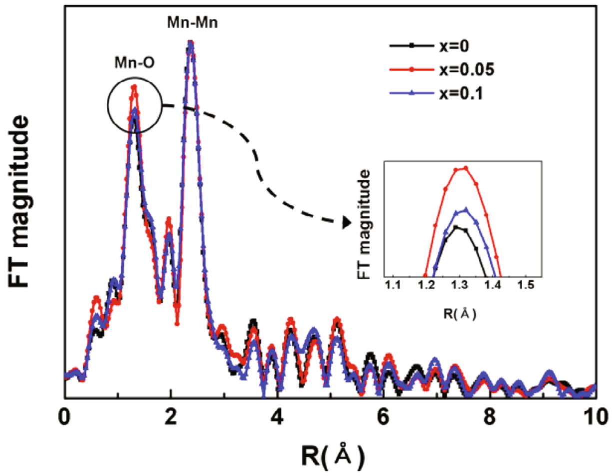

Fig. 16. (Color online) Fourier-transformed EXAFS spectra of $LiSn_{x/2}Mn_{2-x}O_4$ thin films. (Copyright 2009 Elsevier B. V [55]).

III. CONCLUSION

This review is focused on developing novel $LiMn_2O_4$-based electrodes for thin film batteries (TFBs) using by Sn substitution. This study provides the most significant breakthrough for the realization of TFBs because it suggests the solution to overcome the current obstacle, the degradation of battery operation caused by Jahn-Teller distortion.

The thin films were galvanostatically cycled at quite high current rates of ≥ 4 C in the voltage range of $4.5 - 3.0$ V. The high load-current and cyclability are critical in this study because the expected applications of our materials are based on small-sized devices such as USNs (ubiquitous sensor networks) and RF-IDs. Therefore, the harsh conditions were used, *i.e.*, the high current rates ≥ 4 C and the wide potential range of $4.5 - 3.0$ V considering the former usage.

As a preliminary study of Sn-substituted $LiMn_2O_4$-based electrode materials, the synthesis with the substituents of SnO and SnO_2 was investigated by using the conventional solid-state reaction. The identification of a $LiMn_2O_4$ single-phase without impurities, implied that synthesized $LiMn_2O_4$-based materials Sn could be incorporated into $LiMn_2O_4$ spinel structure.

In an initial study on high cyclability electrode films, new spinel Sn-substituted $LiMn_2O_4$ thin films were fabricated by means of pulsed laser ablation from the targets in a preliminary study. Accordingly, Sn^{2+}-substituted thin films were prepared by using PLD. The $LiSn_{0.0125}Mn_{1.975}O_4$ thin films possessed a larger capacity of ~120 mAh/g due to the Mn-deficient structure and a higher cyclability of $> 81\%$ at 4 C after 90 cycles due to the increase in the valence of Mn, or compared to the capacity of ~100 mAh/g and the cyclability of ~65% for $LiMn_2O_4$ thin films, respectively. The near-edge x-ray absorption fine structure (NEXAFS) analysis suggested feasible criteria for determining the Sn content for substitution and the initiation of cyclability degradation.

The Sn-substituted $LiMn_2O_4$ thin films were fabricated by means of solution deposition utilizing Sn (II) acetate with a focus on the appropriate Sn content and the mechanism for Sn substitution. The appropriate Sn content was $x \leq 0.05$ in $LiSn_x/2Mn_{2-x}O_4$. The improved cyclability of solution-deposited $LiSn_{0.025}Mn_{1.95}O_4$ thin films was 77% at a current rate of 10 C after 500 charge-discharge cycles, compared to 12% for $LiMn_2O_4$. The superior cyclability was proven to be attributed to the increase in the average valence state of manganese and the decrease in MnO_6 octahedral distortion in the spinel structure, which had been demonstrated by using the extended X-ray absorption fines structure (EXAFS) identifying Mn(Sn)−Mn and Mn(Sn)−O bonds. The distribution ratios of Mn^{3+}/Mn^{4+} and Sn^{2+}/Sn^{4+} were determined by deconvoluting the Mn and the Sn narrow scanned X-ray photoelectron spectroscopy (XPS) profiles. With the X-ray diffractions patterned for the as-deposited and the cycled thin-film electrodes, the trade-off effects of Sn^{2+} and Sn^{4+} on the valence state of Mn were examined. Beyond the optimal composition of $LiSn_{0.025}Mn_{1.95}O_4$, further Sn substitutions had an insignificant influence on the cycling performance. Apparent precipitation of SnO_2 and SnO was observed for the excessively Sn-substituted thin films after the cycling test.

ACKNOWLEDGMENTS

J.-W.C. gratefully acknowledges the Korea Institute of Science and Technology for financial assistance through the project of K-GRL(2Z04060) and Future Resource Program(2E24770).

REFERENCES

[1] K. Mizushima, P. C. Jones, P. J Wiseman and J. B. Goodenough, Mater. Res. Bull. **15**, 783 (1980).

[2] H. Xia, L. Lu and G. Ceder, J. Power Sources **159**, 1422 (2006).

[3] N. Ariel, G. Ceder, D. R. Sadoway and E. A. Fitzgerald, J. Appl. Phys. **98**, 023516 (2005).

[4] J. P. Maranchi, A. F. Hepp and P. N. Kumta, Mater. Sci. Eng. B **116**, 327 (2005).

[5] F. K. Shokoohi, J. M. Tarascon, B. J. Wilkens, D. Guyomard and C. C. Chang, J. Electrochem. Soc. **139**, 1845 (1992).

[6] H. S. Hwang, S. H. Oh, H. S. Kim, W. I. Cho, B. W. Cho and D. Y. Lee, Electrochim. Acta **50**, 485 (2004).

[7] J. Ma and Q.-Z. Qin, J. Power Sources **148**, 66 (2005).

[8] M. M. Thackeray, Prog. Solid St. Chem. **25**, 1 (1997).

[9] M. M. Thackeray, W. I. F. David, P. G. Bruce and J. B. Goodenough, Mat. Res. Bull. **18**, 461 (1983).

[10] R. D. Shannon, Acta Crystallogr. A **32**, 751 (1976).

[11] B. J. Hwang, R. Santhana, D. G. Liu and Y. W. Tsai, J. Power Sources **102**, 326 (2001).

[12] H. Ahan, H. Göktepe and Patat, A. Materials science-Poland **28**, 4 (2010).

[13] D. Arumugam, and G.P. Kalaignan, J. Electroanalytical. chem. **648**, 154 (2010).

[14] C. H. Shen, R. S. Liu, R. Gundakarama, J. M. Chenb, S. M. Huangc, J. S. Chenc and C.M. Wangc, J. Power Sources **102**, 21 (2001).

[15] H. Xiangming, L. Jianjun, C. Yan, W. Yaowu, Y. Jierong, J. Changyin and W. Chunrong, J. Power Sources **150**, 216 (2005).

[16] S. Gui-Ming, W. Yu-Jin and Y. Zhou, J. Power Sources **128**, 270 (2004).

[17] H. Xiangming, L. Jianjun, C. Yan, W. Yaowu, Y. Jierong, J. Changyin and W. Chunrong, Solid state ionics **176**, 2571 (2005).

[18] D. Arumugam, G. P. Kalaignan and P. Manisankar, Solid state ionics **179**, 580 (2008).

[19] R. Singhala, S. R. Dasb, M. S. Tomara, O. Ovideoa, S. Nietoc, R. E. Melgarejo and R. S. Katiyar, J. Power Sources **164**, 857 (2007).

[20] S. Gui-Ming, W. Yu-Jin and Y. Zhou, Materials Chemistry and Physics **87**, 162 (2007).

[21] Y. F. Yuan, H. M. Wub, S. Y. Guo, J. B. Wu, J. L. Yang, X. L. Wang and J. P. Tu, Applied Surface Science **255**, 2225 (2008).

[22] L. Huiyong, D. Ganqun and G. Yonglang, J. Rare Earths **26**, 722 (2008).

[23] C. S.Yoon, C. K. Kim and Y. K. Sun, J. Power Sources **109**, 234 (2002).

[24] D. Arumugam, G. P. Kalaignan, K. Vediappan and C. W. Lee, Electrochim. Acta **55**, 8439 (2010).

[25] Y. Uchimoto, M. Kunuhata and Y. Yao, Jpn. J. Appl. Phys. **38-1**, 111 (1999).

[26] T. Yao, Y. Uchimoto, M. Kinuhata, T. Inagaki and H. Yoshida, Solid State Ionics **132**, 189 (2000).

[27] JCPDS 35-0782.

[28] M. Wakihara, Mater. Sci. Eng. R **33**, 109 (2001).

[29] N. J. Dudney, J. B. Bates, R. A. Zuhr, S. Young, J. D. Robertson, H.P. Jun and S. A. Hackney, J. Elecctrochem. Soc. **146**, 2455 (1999).

[30] K. A. Striebel, C. Z. Deng, S. J. Wen and E. J. Cairns, J. Electrochem. Soc. **143**, 1821 (1996).

[31] A. Rougier, K. A. Striebel, S. J. Wen, T. J. Richardson, R. P. Reade and E. Cairns, J. Appl. Surf. Sci. **134**, 107 (1998).

[32] C. Julien, E. Haro-Poniatowski, M. A. Camacho-Lopez, L. Escobar-Alarcon and J. Jimenez, J. Mater. Sci. Eng. B **72**, 36 (2000).

[33] D. Singh, R. Houriet, R. Giovannini, H. Hofmann, V. Craciun and R. K. Singh, J. Power Sources **97-98**, 826 (2001).

[34] C. Ouyang, H. Deng, Z. Ye, M. Lei and L. Chen, Thin Solid Films **503**, 268 (2006).

[35] H. Otsuji, K. Kawahara, T. Ikegami and K. Ebihara, Thin Solid Films **506**, 120 (2006).

[36] T. Dumont, T. Lippert, M. Doebeli, H. Grimmer, J. Ufheil, P. Novak, A. Wuersig, U. Vogt and A. Wokaun, Appl. Surf. Sci. **252**, 4902 (2006).

[37] S. B. Tang, M. O. Lai, L. Lu and S. J. Tripathy, Solid State Chem. **179**, 3831 (2006).

[38] O. M. Hussain, K. H. Krishna, V. K. Vani and C. M. Julien, Solid State Ionics **13**, 455 (2007).

[39] M. M. Thackeray, Y. Shao-Horn, A. J. Kahaian, K. D. Kepler, E. Skinner, J. T. Vaughey and S. A. Hackney, Electrochem. Solid State **1**, 7 (1998).

[40] Y. Gao and J. R. Dahn, J. Electrochem. Soc. **143**, 100 (1996).

[41] D. W. Shin, J. W. Choi, W. S. Cho and S. J. Yoon, J. Electroceram. **23**, 200 (2009).

[42] C. -L. Li and Z. -W. Fu, Electrochim. Acta **52**, 6155 (2007).

[43] A. Caballero, M. Cruz, L. Hernán, M. Melero, J. Morales and E. R. Castellón, J. Electrochem. Soc. **152**, A552 (2005).

[44] H. M. Wu, J. P. Tu, Y. F. Yuan, Y. Li, X. B. Zhao and G. S. Cao, Mat. Sci. Eng. B **119**, 75 (2005).

[45] J. M. Paulsen and J. R. Dahn, Chem. Mater. **11**, 3065 (1999).

[46] M. Winter, J. O. Besenhard, M. E. Spahr and P. Novák, Adv. Mater. **10**, 725 (1998).

[47] T.-T. Fang and H.-Y. Chung, J. Am. Ceram. Soc. **91**, 342 (2008).

[48] M. J. Iqbal and Z. Ahmad, J. Power Sources **179**, 763 (2008).

[49] X. He, W. Pu, Y. Cai, C. Jiang and C Wan, Solid State Ionics **12**, 73 (2006).

[50] J. A. Tossell, D. J. Vaughan and K. H. Johnson, Am. Mineral. **59**, 319 (1974).

[51] R. S. Liu, L. Y. Jang, J. M. Chen, Y. C. Tsai, Y. D. Hwang and R. G. Liu, J. Solid State Chem. **128**, 326 (1997).

[52] D. W. Shin J. W. Choi W. K. Choi and S. J. Yoon, Appl. Phys. Lett. **93**, 064101 (2008).

[53] S. O. Kucheyev *et al.*, J. Phys. Rev. B **69**, 245102 (2004).

[54] T. Doi, M. Inaba, Y. Iriyama, T. Abe and Z. Ogumi, J. Electrochem. Soc. **155**, A20 (2008).

[55] D. W. Shin, J. W. Choi, W. K. Choi and S. J. Yoon , Electrochem. Comm. **11**, 695 (2009).

[56] J. M. Tarascon, W. R. McKinnon, F. Coowar, T. N. Bowner, G. Amatucci and D. Guromard, J. Electrochem. Soc. **141**, 1421 (1994).

[57] W.-K. Choi, H.-J. Jung and S.-K. Koh, J. Vac. Sci. Technol. A **14**, 359 (1996).

[58] M. Kaneko, S. Matsuno, T. Miki, M. Nakayama, H. Ikuta, Y. Uchimoto, M. Wakihara and K. Kawamura, J. Phys. Chem. B **107**, 1727 (2003).

[59] P. Aitchison, B. Ammundsen, J. Rozière, G. R. Burns and D.J. Jones, Solid State Ionics **176**, 813 (2005).

[60] B. J. Hwang, Y. W. Tsai, R. Santhanam, Y. W. Wu, S. G. Hu, J. F. Lee and D. G. Liu, J. Power Sources **123**, 206 (2003).